FULL PAPER

Photoluminescence

ADVANCED
FUNCTIONAL
MATERIALS

www.afm-journal.de

Photoluminescent Arrays of Nanopatterned Monolayer MoS$_2$

Grace G. D. Han, Kun-Hua Tu, Farnaz Niroui, Wenshuo Xu, Si Zhou, Xiaochen Wang, Vladimir Bulović, Caroline A. Ross, Jamie H. Warner, and Jeffrey C. Grossman*

Monolayer 2D MoS$_2$ grown by chemical vapor deposition is nanopatterned into nanodots, nanorods, and hexagonal nanomesh using block copolymer (BCP) lithography. The detailed atomic structure and nanoscale geometry of the nanopatterned MoS$_2$ show features down to 4 nm with nonfaceted etching profiles defined by the BCP mask. Atomic resolution annular dark field scanning transmission electron microscopy reveals the nanopatterned MoS$_2$ has minimal large-scale crystalline defects and enables the edge density to be measured for each nanoscale pattern geometry. Photoluminescence spectroscopy of nanodots, nanorods, and nanomesh areas shows strain-dependent spectral shifts up to 15 nm, as well as reduction in the PL efficiency as the edge density increases. Raman spectroscopy shows mode stiffening, confirming the release of strain when it is nanopatterned by BCP lithography. These results show that small nanodots (≈19 nm) of MoS$_2$ 2D monolayers still exhibit strong direct band gap photoluminescence (PL), but have PL quenching compared to pristine material from the edge states. This information provides important insights into the structure–PL property correlations of sub-20 nm MoS$_2$ structures that have potential in future applications of 2D electronics, optoelectronics, and photonics.

1. Introduction

Monolayer transition metal dichalcogenides (TMDs), such as MoS$_2$ and WS$_2$, are direct band gap semiconductors and offer new opportunities in electronics, optoelectronics, and photonics beyond graphene.[1–3] A key aspect in realizing the potential of 2D materials is the ability to create nanoscale structures with monolayer thickness, either by lithographically patterning a 2D film after growth, or by growing the 2D material directly as nanoscale dots or ribbons.[4–6] It is also important to understand how nanoscale patterning processing can change the electronic and optical properties of the 2D material. In graphene, nanoribbons have been synthesized by both approaches, with the latter accomplished by the high temperature reaction of molecular based precursors on a substrate[7,8] and the unzipping of carbon nanotubes.[9–12] Chemical and solvothermal exfoliation of bulk MoS$_2$ has led to the production of small nanoparticles of MoS$_2$ with modified optical properties.[13–17] The recent advancements in chemical vapor deposition (CVD) growth of large-area 2D TMD monolayer sheets offers an ideal platform for lithography and etching that will be compatible with electronic and optoelectronic device applications.

Patterning of 2D materials is often achieved using resist-based electron-beam[18,19] and optical lithography methods,[20] direct patterning by focused ion beams (Ga[21,22] and He),[23–25] energetically preferred chemical etching,[26,27] nanoprobe cutting[28] and block copolymer (BCP) lithography.[29] Block copolymers, which consist of two or more incompatible blocks, microphase separate below their order–disorder temperature into periodic arrays of microdomains such as spheres, cylinders, or lamellae.[30–32] Thin films of BCPs thus enable nanoscale patterning of various materials including silicon,[33] silicon nitride,[34] and metal oxides[35,36] for use in air–gap structures, capacitors, field effect transistors, memories, and other devices.[37] In particular, BCPs have been used to pattern graphene into nanoribbons[29,38,39] with sub-10 nm widths for use in transistors, quantum dots,[40] as well as hexagonal nanomesh.[41] Thin films of BCPs have been employed in templating the growth of 3D crystalline nanoparticles and nanowires of TMDs.[42,43] To date there is little work on the direct patterning of 2D monolayer TMDs with BCPs to generate nanostructures and the comprehensive study of the impact this has on the direct band gap photoluminescence emission from monolayer TMDs such as MoS$_2$. Furthermore, the detailed atomic structure of BCP nanopatterned 2D structures has yet to be examined in detail, which is important to determine the accurate structure and effects of the etching process.

Dr. G. G. D. Han, Dr. K.-H. Tu, Prof. C. A. Ross, Prof. J. C. Grossman
Department of Materials Science and Engineering
Massachusetts Institute of Technology
77 Massachusetts Avenue, Cambridge, MA 02139, USA
E-mail: jcg@mit.edu
Dr. F. Niroui, Prof. V. Bulović
Department of Electrical Engineering and Computer Science
Massachusetts Institute of Technology
77 Massachusetts Avenue, Cambridge, MA 02139, USA
W. Xu, S. Zhou, X. Wang, Prof. J. H. Warner
Department of Materials
University of Oxford
Parks Road, Oxford OX1 3PH, UK

The ORCID identification number(s) for the author(s) of this article can be found under https://doi.org/10.1002/adfm.201703688.

**ADVANCED
SCIENCE NEWS**
www.advancedsciencenews.com

**ADVANCED
FUNCTIONAL
MATERIALS**
www.afm-journal.de

Here, we explore the fundamental properties and structure of MoS_2 monolayers when patterned into small nanostructured features. This is achieved using a combination of scanning electron microscopy (SEM), atomic force microscopy (AFM), and aberration corrected scanning transmission electron microscopy (STEM) to resolve the atomic and nanoscale structure of nanodots, nanorods and nanomesh features in BCP-patterned MoS_2 monolayers grown by CVD. We then compare the photoluminescence properties of the nanopatterened regions with nonpatterned regions of MoS_2 to understand the impact that nanostructuring has on the PL behavior. This provides important insights into the modifications that can be expected in monolayer 2D TMDs when reduced to nanoscale dimensions with increased edge density, which has implications for future optoelectronic applications involving nanoscale MoS_2 monolayers.

2. Results and Discussion

MoS_2 was grown using CVD, with triangular shaped domains on the scale of 10–100 μm randomly distributed across a 1 cm silicon wafer with 300 nm silicon oxide layer. A schematic illustration of the flow-chart process used to create the nanodots in MoS_2 is presented in **Figure 1**a. Poly(methyl methacrylate) (PMMA) is first spin-coated over the entire substrate to act as a sacrificial layer for lift-off in the final stages to remove any

residual BCP. Next the substrate is coated with a polystyrene-*block*-polydimethylsiloxane (PS-*b*-PDMS) layer which self-assembles into periodic arrays of PDMS spheres embedded in a PS matrix through a toluene vapor annealing process, as previously reported.[44–46] PS-*b*-PDMS is chosen for the fabrication of a self-organized nanotemplate because of its desirable etch selectivity, the formation of highly ordered features, and its scalability to small dimensions due to its high Flory–Huggins interaction parameter (χ).[47] Oxygen plasma is then used to preferentially etch through the PS region of the BCP and remove the underlying PMMA and MoS_2. The exposure of PDMS to the oxygen plasma results in the conversion to a silica-like oxidized PDMS (ox-PDMS)[48,49] which is immobilized and selectively covers the underlying PMMA layer and MoS_2. The remaining PMMA and ox-PDMS are then removed in a lift-off process by submerging the stack in acetone for at least 4 h. Figure 1b,c shows schematic illustrations of a nanopatterned MoS_2 monolayer domain composed of ≈20 nm dots by the BCP-templated lithography.

The formation of nanopatterns before lift-off of the etch mask was confirmed by SEM as shown in **Figure 2**. As-grown 10–100 μm MoS_2 domains with uniform contrast (Figure 2a) were covered first by a PMMA layer and then by a BCP film that generates hexagonally ordered spherical PDMS microdomains within a PS matrix, and a PDMS surface wetting layer, as previously reported.[50] After removing the PDMS wetting layer then etching the PS matrix in oxygen, the remaining oxidized PDMS microdomains serve as an etch mask, as seen in Figure 2b–d.
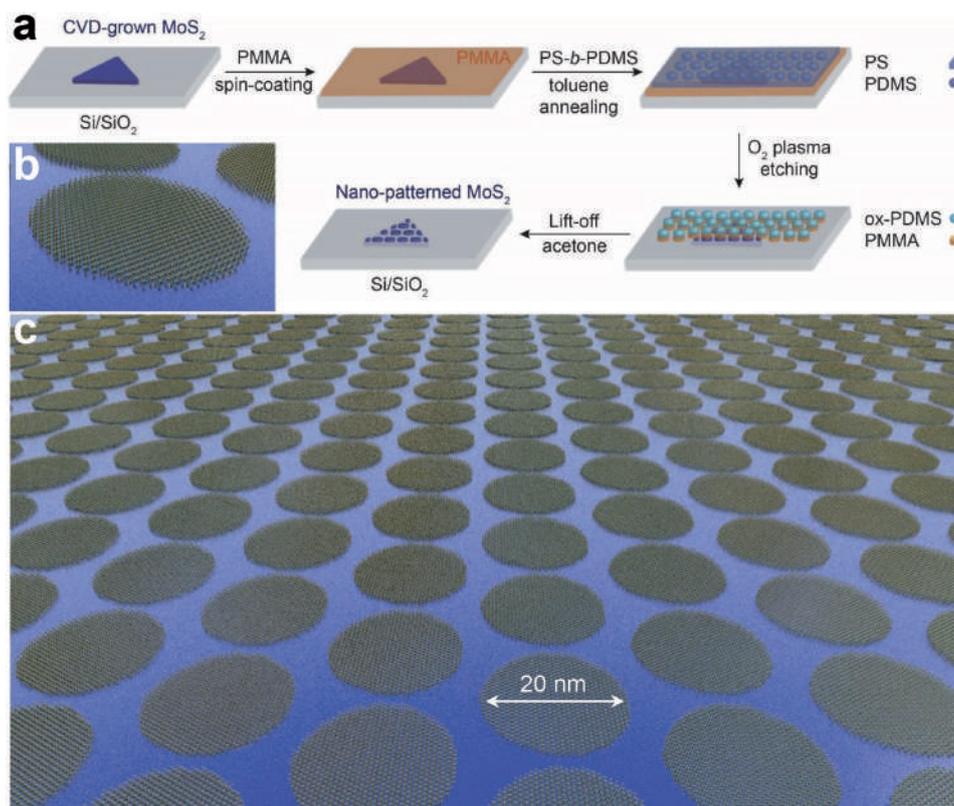
Figure 1. Schematic illustration of the BCP patterning process for nanodot fabrication in MoS_2. a) Flow chart for nanopatterning procedure of monolayer MoS_2 domains using PS-*b*-PDMS block copolymers as an etch mask. Schematics of b) monolayer MoS_2 patterned in the shape of dots and c) an array of nanodots (≈20 nm in diameter) formed as a result of BCP lithography.

**ADVANCED
SCIENCE NEWS**
www.advancedsciencenews.com

**ADVANCED
FUNCTIONAL
MATERIALS**
www.afm-journal.de
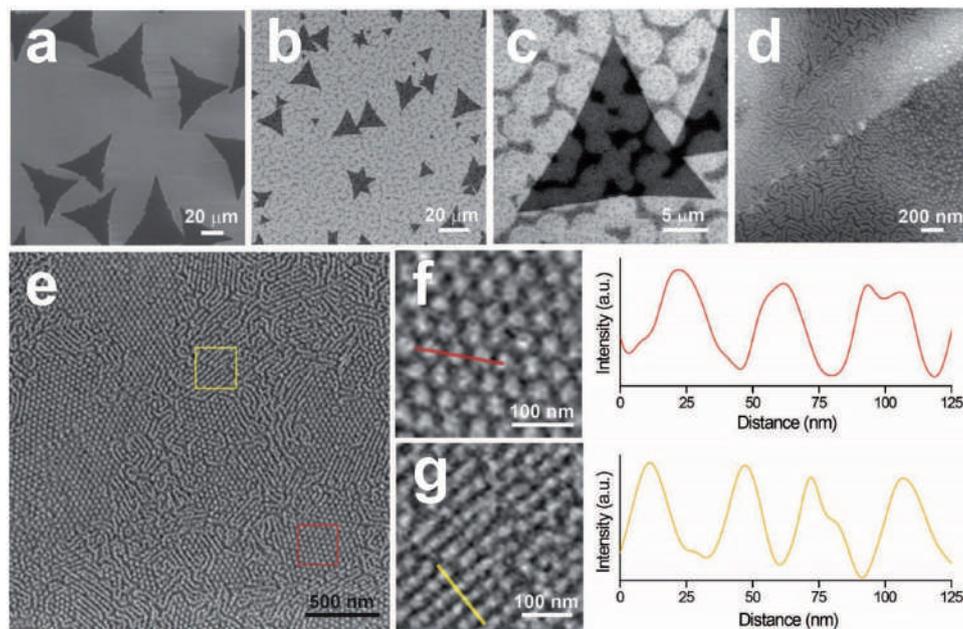
Figure 2. SEM characterization of the nanopatterned MoS$_2$ fabricated by BCP and oxygen plasma etching. a) SEM image of the as-grown MoS$_2$ before BCP patterning. b) SEM image showing a large area of the sample covered with silica-like ox-PDMS nanostructures after oxygen plasma etching of BCP patterns. c) SEM image of a single triangular MoS$_2$ domain with ox-PDMS pattern. The dark micron-scale patterns represent the areas covered with ox-PDMS rods that are generated by the BCP bilayer. Lighter regions are covered with ox-PDMS dots that are formed by the BCP monolayer. d) SEM image with higher magnification showing the edges of MoS$_2$ domains (dark contrast) with the ox-PDMS mask covering the entire substrate. e) SEM image of the detailed structure of the ox-PDMS mask on MoS$_2$, showing the presence of well-ordered dot and rod arrays (light contrast). f) Magnified view of the region indicated with the red box in (e) showing hexagonally packed ox-PDMS dots and the line profile of dots. g) Magnified view of the region indicated with the yellow box in (e) showing ox-PDMS rods and their line profile. The average diameter or width of dots and rods is 16–20 nm.

Terracing happened during the annealing, as the BCP film thickness is not commensurate with the desired thickness of a monolayer of PDMS microdomain. While a monolayer region shows a dot array, the region with thicker BCP film would have a second layer of dots positioned on the gap of first layer dots, leading to a nanorod-like array after etching. Increased thickness of the BCP films produced a nanomesh pattern after etching and when too thick the MoS$_2$ was left unpatterned due to the lack of oxygen plasma penetration in the time interval used. The substrate is completely covered by the ox-PDMS pattern, displaying contrast between the areas covered either with rods (appear darker) or dots (lighter), which is clearly seen in Figure 2d. The BCP is untemplated, and the pattern shows short-range order, with areas of rods and dots due to BCP thickness variations caused by terracing. Although not applied here, long range order can be imposed using topographical templates to guide the BCP self-assembly.[51]

Figure 2e shows coexisting ox-PDMS dots and rods with brighter contrast relative to the substrate. The dimensions of the features were analyzed in Figure 2f,g by measuring the line profiles of hexagonally ordered dots and parallel rods. The average diameter of the dots (20 nm) and the width of rods (16 nm) were determined by measuring the full width at half maximum of the line profiles. The average period of each pattern (35.5 nm for dots and 30 nm for rods) and varying lengths of the rods (60–320 nm, commonly ≈200 nm) were also measured by analyzing the SEM images.

Next we demonstrate that the nanopatterned monolayer TMDs can remain on the substrate after the removal of the lithographic mask. Acetone is used instead of NMP for the PMMA removal in order to prevent the detachment of TMD domains by the NMP. **Figure 3**a,b shows the optical microscope images of CVD-grown pristine MoS$_2$ domains and those covered by the ox-PDMS after oxygen plasma etching, respectively. The bright microscale patterns in Figure 3b consist of rods, and the rest of the substrate is instead covered with dots. After lifting off the PMMA sacrificial layer and the overlying ox-PDMS by immersing the substrate in acetone, we obtained mainly two types of MoS$_2$ domains as in Figure 3c,d. The former exhibits mostly unvarying contrast within a domain, similar to a pristine monolayer, whereas the latter displays microscale patterns that resemble the arrangement of the ox-PDMS mask shown in Figures 3b and 2c. The uniform domains were found near the edges of the substrate where the thicker spin-coated BCP film produced mainly rods and only a few dots. The domains in Figure 3d are present in the center of the substrate where a thinner BCP coating is formed and produces the mixture of ox-PDMS dots and rods after oxygen plasma etching. A SEM image of such domains (Figure 3e) exhibits both nanodots and nanorods of monolayer MoS$_2$, and the measured dimensions of the nanopatterns in Figure 3f,g are consistent with those of the ox-PDMS structures in Figure 2. The uniform domains as in Figure 3c are composed primarily of rod-shaped structures with a small number of nanodots interspersed as revealed by SEM (Figure 3h), similar to previously reported patterns formed with a PS-*b*-PDMS polymer.[52] The ratio of areas covered by dots and rods is determined by the thickness of the deposited BCP and affects the optical contrast of the nanostructured domains.

**ADVANCED
SCIENCE NEWS**

www.advancedsciencenews.com

**ADVANCED
FUNCTIONAL
MATERIALS**

www.afm-journal.de
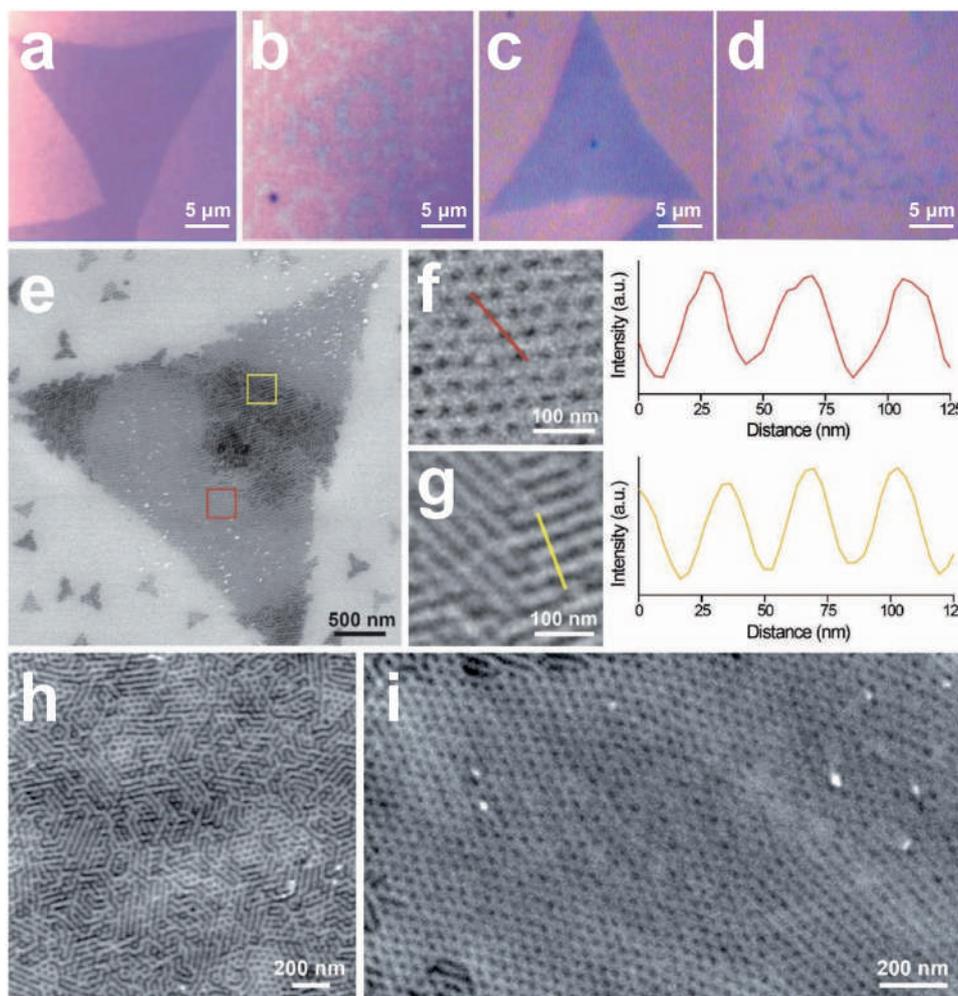
Figure 3. Optical microscope and SEM characterization of nanostructured MoS_2 after the lift-off process. Optical microscope images of monolayer MoS_2 domains that are a) pristine (as-grown), b) covered with an ox-PDMS mask layer, c) nanopatterned mostly with rods after the lift-off process, and d) nanopatterned with dots and rods. e) SEM image of a nanopatterned monolayer MoS_2 domain comprised of MoS_2 dots and rods, as the domain in (d). f) Magnified view of the region indicated with the red box in (e) showing hexagonally packed MoS_2 dots and the line profile of dots. g) Magnified view of the region indicated with the yellow box in (e) showing MoS_2 rods and their line profile. MoS_2 is seen darker relative to the SiO_2 substrate. The average diameter or width of MoS_2 dots and rods is 16–20 nm. h) A domain patterned mainly in the shape of rods with smaller number of dots filling the space between rods, corresponding to the optical image (c). i) Larger area of MoS_2 nanodot arrays with a hexagonal order. Bright dots represent ox-PDMS that remained after the lift-off process.

The hexagonally ordered nanodots form continuous arrays in a large area up to 2 µm in width (Figures 3e,i), which confirms the BCP lithographic method for creating nanostructured TMDs. Figures S1 and S2 of the Supporting Information show additional SEM images of MoS_2 at various scales from ≈100 to ≈10 µm that are patterned with nanodots, nanorods, and hexagonal nanomesh, depending on the thickness of the BCP film.

AFM topography in **Figure 4** corroborates the results shown in Figure 3. We probed nanostructured MoS_2 regions and ox-PDMS that was partially left behind after the lift-off process (Figure 4a). The center of the region was examined at higher magnification where coexisting nanodots and nanorods were found (Figure 4b). The height profile across the step edge of the MoS_2 domain on the substrate indicates a monolayer thickness (Figure 4c). The magnified regions from Figure 4b show the detailed structures of nanodots (Figure 4d) and nanorods

(Figure 4e) that are well defined on the substrate. High-magnification topography of a region within Figure 4a is shown in Figure 4f which illustrates both dot- and rod-shaped MoS_2 structures, and their height profiles confirm they are a monolayer thick. Figure S3 of the Supporting Information contains additional AFM images of MoS_2 monolayers that are patterned with nanodots, nanorods, and hexagonal nanomesh, resulting from various thickness of BCP films.

To investigate the atomic structure and nanoscale features of the nanopatterned MoS_2, we transferred it to a TEM grid that already had large-area monolayer WS_2 suspended across holes. This enables the MoS_2 nanodots and nanorods to be easily imaged against the low contrast WS_2 substrate using annular dark field scanning transmission electron microscopy (ADF-STEM). **Figure 5**a shows several MoS_2 nanodots arranged in a periodic pattern on the WS_2 surface, with a higher

**ADVANCED
SCIENCE NEWS**
www.advancedsciencenews.com

**ADVANCED
FUNCTIONAL
MATERIALS**
www.afm-journal.de
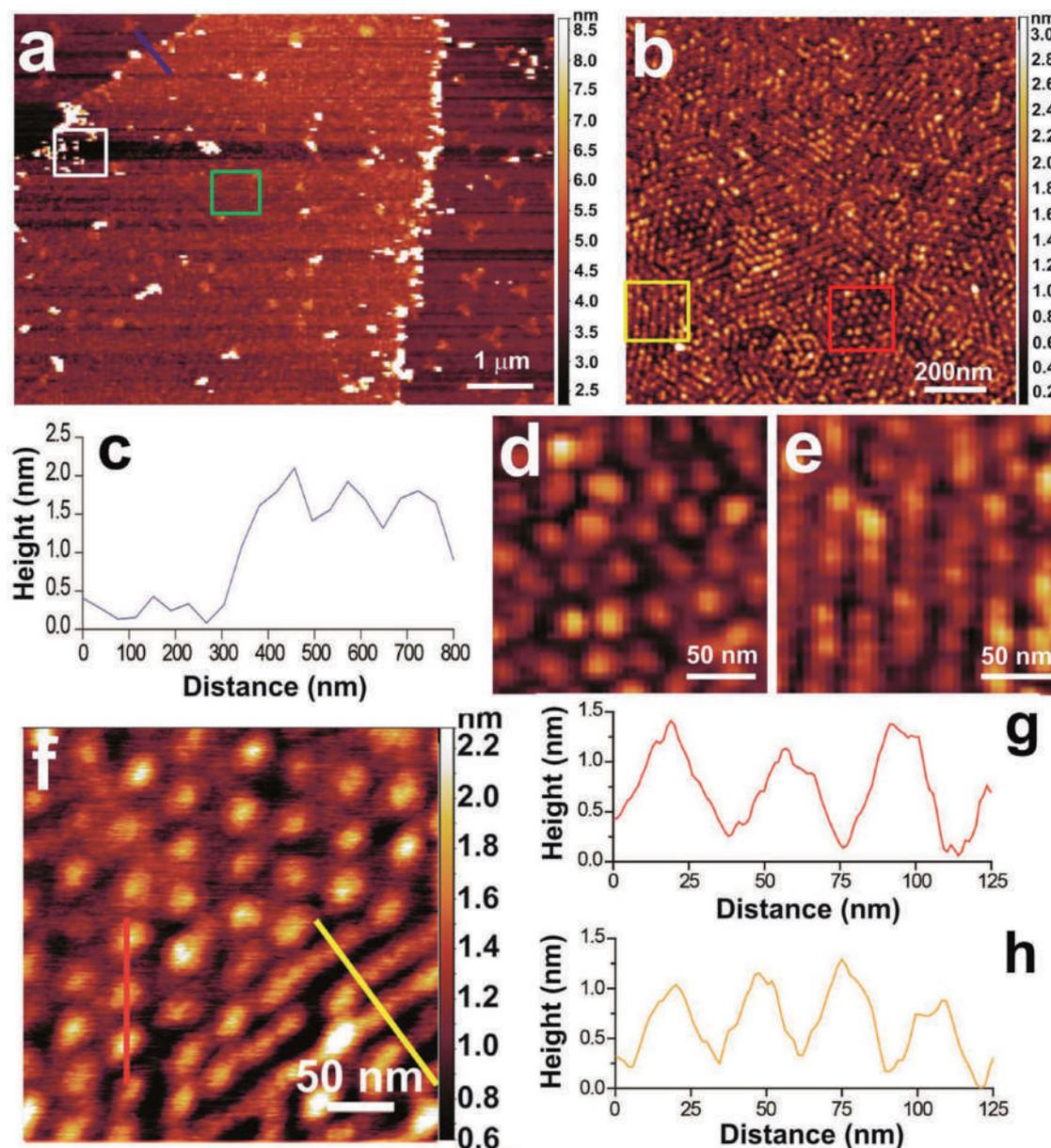
Figure 4. AFM characterization of nanostructured MoS_2 after the lift-off process. a) Low-magnification AFM topography of nanopatterned monolayer MoS_2. b) Representative mid-magnification topography of the outlined area in a) (green) in the center of the MoS_2 domain. c) Height profile of the denoted section (blue line) in (a) showing a monolayer thickness of MoS_2 on the SiO_2 substrate. d) Magnified view of the region indicated with the red box in (b) showing nanodots. e) Magnified view of the region indicated with the yellow box in b) showing nanorods. f) Representative high-resolution topography of the outlined area in a) (white) near the edge of the MoS_2 domain, showing individual MoS_2 dots and rods. Height profiles from the respective red and yellow lines indicated in f) for g) nanodots and h) nanorods. The average height of ≈1 nm corresponds to a monolayer thickness, and the average size of the nanopatterns of 16–20 nm matches the SEM characterization.

magnification image of a single nanodot shown in Figure 5b. The nanodots are round with no visible faceting, indicating that the shape is mainly defined by the BCP mask during etching. The inset of Figure 5a shows the FFT from the region in the yellow box, and two sets of reflections are indicated for the MoS_2 and WS_2. A Moire pattern is visible in the ADF-STEM image in Figure 5b, and when the WS_2 lattice is removed by a negative mask filter of the FFT and inverted, the lattice from only the MoS_2 nanodot is seen in Figure 5c. Figure 5d shows the region from the yellow box in Figure 5b, and after removing

the WS_2 lattice by FFT filtering, the lattice of the MoS_2 is visible without major crystal defects, appearing uniform and regular (Figure 5e). The diameter of the MoS_2 nanodot in Figure 5c is measured as ≈19 nm from the line profile taken across the yellow line shown in Figure 5f. The diameter of eleven different MoS_2 nanodots were measured and shown in Figure 5g, with an average of 18.7 nm. Vertically stacked $MoS_2:WS_2$ layers are known to create type II heterostructure with rapid charge transfer, and the images in Figure 5 demonstrate that in principle it is possible to create local periodic variations of

**ADVANCED
SCIENCE NEWS**

www.advancedsciencenews.com

**ADVANCED
FUNCTIONAL
MATERIALS**

www.afm-journal.de
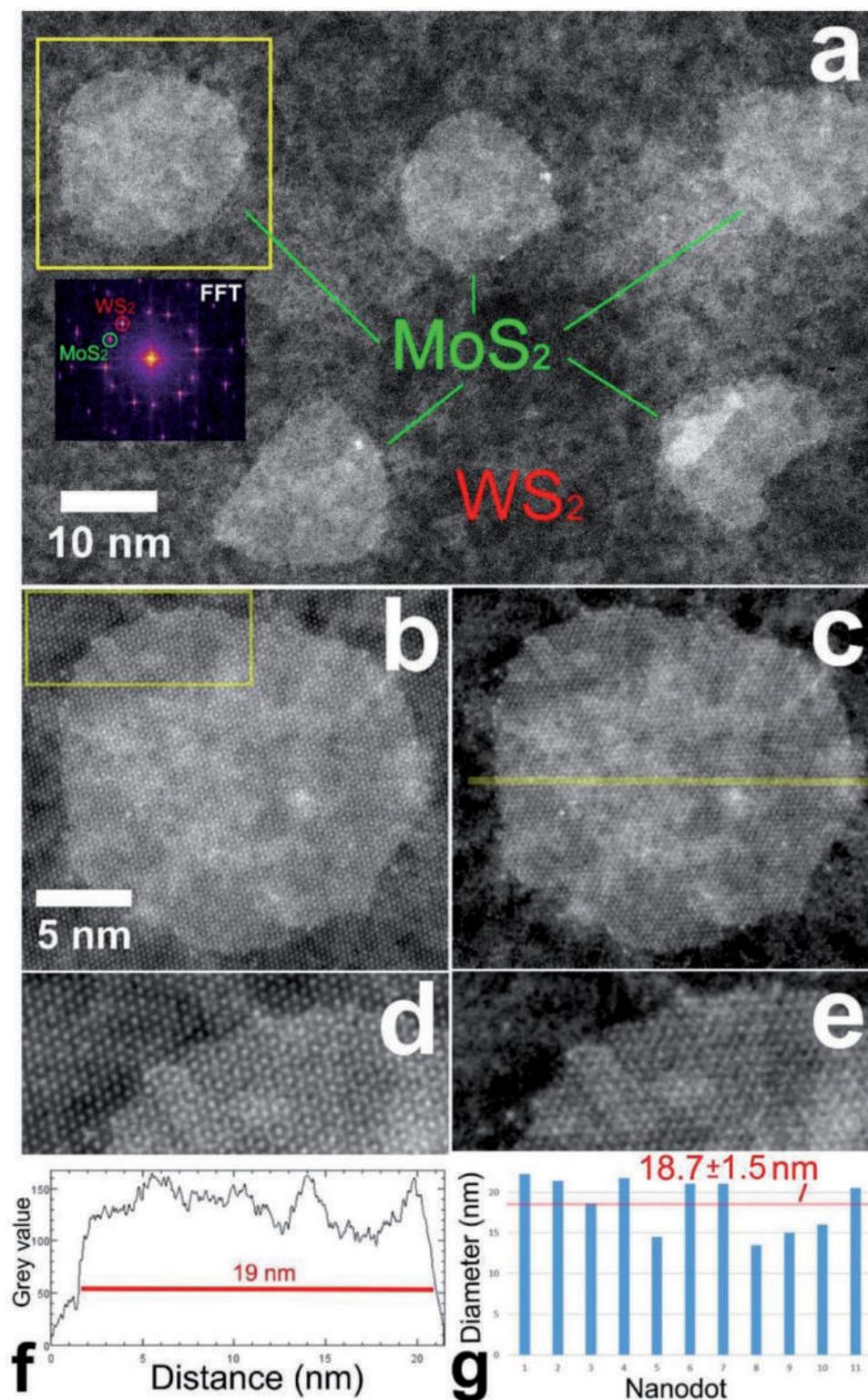
Figure 5. ADF-STEM images of MoS_2 nanodots on top of monolayer WS_2. a) ADF-STEM image showing several MoS_2 nanodots on the surface of WS_2 arranged in a periodic pattern. Inset shows the FFT from the yellow boxed area and reveals two sets of reflections associated with MoS_2 and WS_2 respectively. b) ADF-STEM image of a single MoS_2 nanodot on WS_2 from the yellow boxed area in (a). The Moire pattern in the MoS_2:WS_2 region is visible. c) Atomic resolution image of the MoS_2 nanodot, where the WS_2 lattice is removed by applying a negative mask filter to the FFT and inverted. d) High magnification ADF-STEM image of the region indicated in the yellow box in (c) and then e) after removing the WS_2 lattice contribution using a negative mask in the FFT and inverting. f) Line profile from the yellow line indicate in (c). g) Histogram showing diameters measured for eleven different MoS_2 nanodots from the ADF-STEM images. Red line indicates average diameter value of 18.7 nm.

ADVANCED
SCIENCE NEWS
www.advancedsciencenews.com

ADVANCED
FUNCTIONAL
MATERIALS
www.afm-journal.de
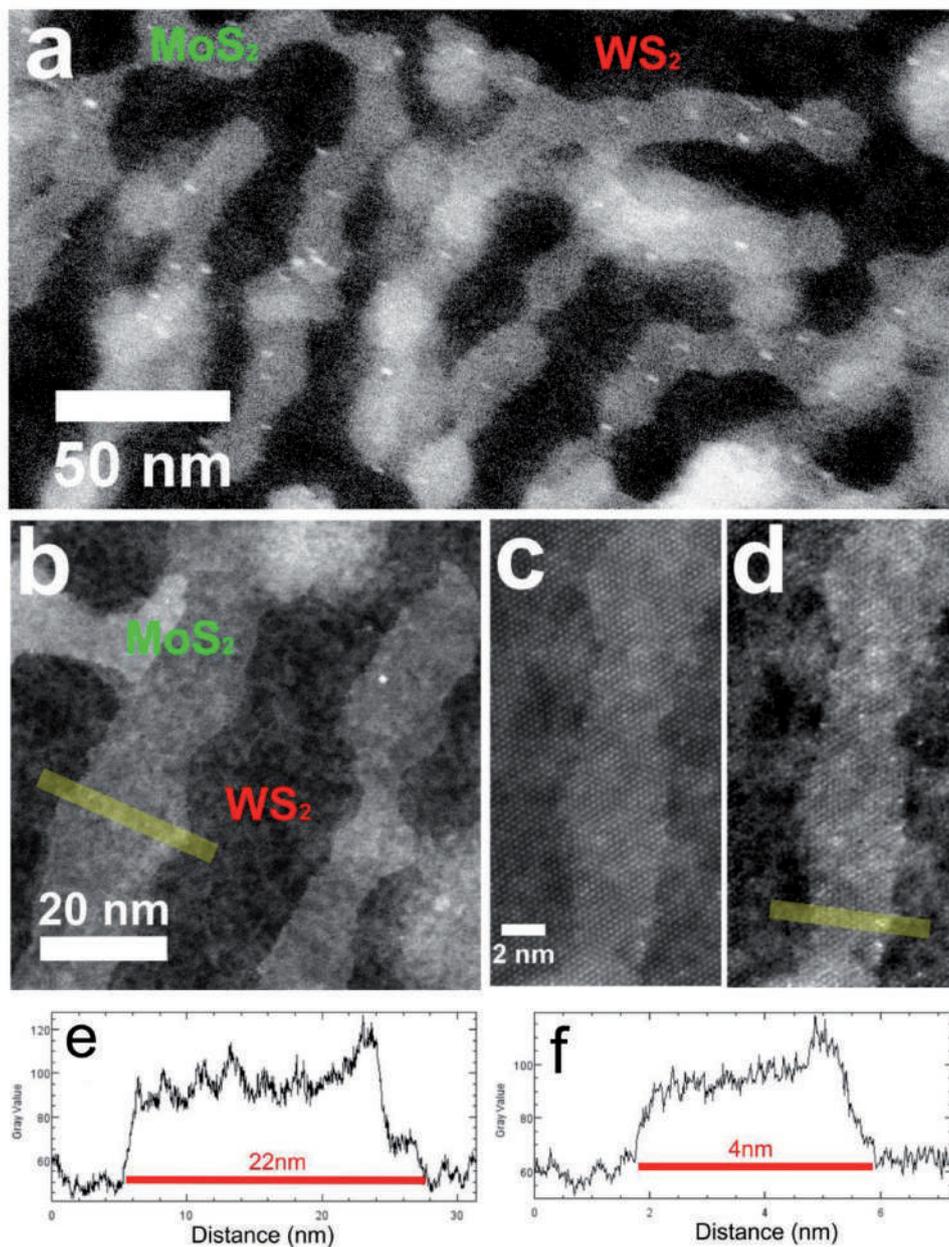
Figure 6. ADF-STEM images of MoS$_2$ nanorods on top of monolayer WS$_2$. a) ADF-STEM image showing several MoS$_2$ nanorods on the surface of WS$_2$ arranged in a periodic pattern. Orange arrow indicates brighter contrast due to some residual ox-PDMS on the surface. b) Higher magnification ADF-STEM image of MoS$_2$ nanorods on WS$_2$. c) Atomic resolution ADF-STEM image of the MoS$_2$ nanorod and d) that with the WS$_2$ lattice removed by applying a negative mask filter to the FFT and inverted. e) Line profile taken from the yellow line indicated in (b). f) Line profile taken from the yellow line indicated in (d).

MoS$_2$ nanodots on WS$_2$ that might have interesting excitonic behavior.

Next we examined the atomic and nanoscale structure of the MoS$_2$ nanorod regions on WS$_2$ using ADF-STEM, similar to Figure 5. The nanorods are expected to have fluctuations in width due to the way the BCP stacks to form the bilayer sections that generate rod features. The ADF-STEM image in **Figure 6**a shows several MoS$_2$ nanorod features with variable constriction widths. Some small amounts of residual ox-PDMS are present (orange arrow in Figure 6a) due to the less aggressive

acetone cleaning procedure used for TEM sample preparation compared to that for the samples on SiO$_2$ substrates, in order to prevent the popping of the fragile suspended WS$_2$ regions that we use as the low contrast support for TEM imaging of these ultra-small monolayer MoS$_2$ features. Higher magnification ADF-STEM images are shown in Figure 6b,c, with widths varying between 4 and 22 nm. The nanorod arrays are fairly uniform and formed in a reproducible way within the area where thick layer of BCP is deposited as seen in Figure 3e,g. The exact widths of the rod structures vary as seen in the high-resolution

ADF-STEM images, and the average width taken from Figure 6a on 15 different parts is ≈12 nm with a standard deviation of ≈3.5 nm. The smallest width of rods measured in our ADF-STEM images was 4 nm. There did not appear to be any crystallographic faceting along the nanorods, again indicating that the shape is determined by the BCP mask. Figure 6d shows the ADF-STEM image of the MoS_2 nanorod after removing the WS_2 lattice contributions using a negative mask filter on the FFT and then inverting the image. The lattice is visible and the crystal structure appears uniform. A detailed atomic resolution ADF-STEM study of regions containing nanomesh structure is presented in Figure S4 (Supporting Information) and shows the holes that make up the nanomesh have a diameter of ≈18 nm, which is similar to the nanodots. The edges of the holes are round and show no signs of crystallographic faceting.

Hexagonal monolayer 2D materials can have either zig-zag or arm-chair edge terminations.[53,54] As shown previously in the literature, in pristine MoS_2 the zig-zag edge terminations along Mo or S directions are energetically favorable.[55–57] The nanostructured MoS_2 in our study is produced by oxygen plasma etching using BCP masks, with the shape mainly determined by the mask profile. Therefore the edge terminations are short range and mixed in the spherical shaped nanodots, with no long range crystallographic ordering at the edge, such as zig-zag faceting.[57] The nanorods also have variable widths and rough edges with no crystallographic long range ordering. The dangling bonds at the edge of 2D TMDs are likely to act as quenching sites for PL emission, but in some special circumstances edges of TMDs can have increased PL compared to their central region.[58] However, the structural origin of this effect has yet to be elucidated. The mixed random edge terminations observed in our nanostructured MoS_2 are likely to have a negative impact on the PL emission due to the lack of periodicity, and this agrees with our observation that the increased edge density causes PL quenching. Further investigation will explore the generation of long range crystallographic edges in the nanostructures through high temperature etching processes, such as annealing in hydrogen gas, which can exploit the energetic differences in chemical stability between edge terminations. This could then be correlated to corresponding changes on PL.

Optical properties of the nanostructured MoS_2 were investigated by photoluminescence (PL) spectroscopy on the selected spots of ≈1 μm size within MoS_2 domains. As-grown pristine MoS_2 domains and those covered by a PMMA layer exhibit identical PL spectra with a peak at 678 nm upon excitation at 514.5 nm (**Figure 7**a), suggesting a negligible effect of the PMMA coating on the photoluminescence of MoS_2 flakes. The parts within the domains covered with ox-PDMS dot etch masks show a blue-shifted PL at 663 nm and those with rods exhibit similar PL at 666 nm. The shift of 12–15 nm can be attributed to the release of the built-in strain in the monolayer MoS_2 that comes from the rapid cooling after the CVD growth process,[59] also supported by Raman spectroscopy measurements. Figure 7b shows the Raman spectra of pristine and nanostructured MoS_2 before the lift-off process. The E^1_{2g} and A_{1g} peaks correspond to in-plane and out-of-plane vibration modes.[60] The pristine MoS_2 shows characteristic peaks at 385 and 406 cm^{-1} for E^1_{2g} and A_{1g} modes, and the spacing between these two peaks of 21 cm^{-1} agrees with the frequency difference measured in high-quality monolayers as previously reported.[61] For the patterned monolayer, both characteristic vibration peaks are blue-shifted, by 1–2 cm^{-1} for the E^1_{2g} mode and 1–4 cm^{-1} for the A_{1g} mode, while the frequency difference between the two peaks decreases by 1 cm^{-1} for nanorods but increases by 3 cm^{-1} for nanodots. A similar degree of stiffening of the E^1_{2g} mode has been reported for monolayer MoS_2 domains transferred onto other substrates (SiO$_2$/Si or h-BN)[62] through a two-step PMMA-assisted process that releases biaxial lattice tensile strain present in the MoS_2 domains directly grown on SiO$_2$. This strain of ≈4% is expected to be entirely released, as also supported by the similar PL peak shifts for exciton and trion of the patterned MoS_2 and those of the transferred MoS_2 domains.[62] A further shift of A_{1g} mode for nanodots, measured before the lift-off process in Figure 7b, is associated with their interaction with the PMMA layer and will be discussed in comparison to the Raman spectra of those after the lift-off in the next paragraphs.

After the lift-off of the PMMA layer and etch mask, the PL and Raman spectra of nanostructured MoS_2 were measured and compared to those of pristine domains. The degree of the blue-shift in PL of ≈15 nm resulting from the nanopatterning was similar to that seen before the lift-off process, indicating the marginal effect of a PMMA layer or an ox-PDMS mask on the PL measurement (Figure 7c). The stiffening of E^1_{2g} and A_{1g} modes by 1.5–2.5 and 0.5–1 cm^{-1}, respectively, was observed for respective dots and rods in Figure 5d, similar to the blue-shift with nanorods before the lift-off (Figure 7b). As a control experiment, the PMMA-assisted transfer of MoS_2 pristine domains onto another SiO$_2$/Si substrate was conducted, and E^1_{2g} and A_{1g} peaks at 387 and 406.5 cm^{-1} were observed on the transferred MoS_2. The Raman shift of two modes overlaps with the other spectra measured from nanostructures after the lift-off, confirming the correlation between the release of strain and the Raman stiffening. Also, the relative intensity of the two modes (A_{1g}/E^1_{2g}) increases by a similar degree for the transferred pristine MoS_2 as for the nanostructured domains.

Since the stiffening of both E^1_{2g} and A_{1g} modes after the lift-off appears consistent regardless of the dimension of the MoS_2 domains, the more significant A_{1g} blue-shift of the nanodots before the lift-off (Figure 7b) implies a doping level change[63,64] supposedly as a result of stronger interaction with the PMMA layer compared to that of other structures. The strong binding of nanodots to the PMMA layer and relatively loose attachment onto the SiO$_2$ substrate has been observed during longer lift-off processes where the nanodots were found detached from the substrate (Figure S5, Supporting Information) as opposed to the remaining nanorod/mesh and to the pristine MoS_2 domains that were protected from O$_2$ plasma etching by a thicker PMMA coating.

The relative PL intensities of as-grown and nanopatterned MoS_2 domains are plotted by normalizing to the Raman A_{1g} mode intensity of each sample, which eliminates other factors from the comparison such as materials quantity, excitation intensity, and local electric field.[2] The Raman intensity and shift of the A_{1g} mode are reported to be more consistent compared to the E^1_{2g} mode with respect to varied density of sulfur vacancies.[65] Figure 7e shows that the PL efficiency of nanodots

**ADVANCED
SCIENCE NEWS**

www.advancedsciencenews.com

**ADVANCED
FUNCTIONAL
MATERIALS**

www.afm-journal.de
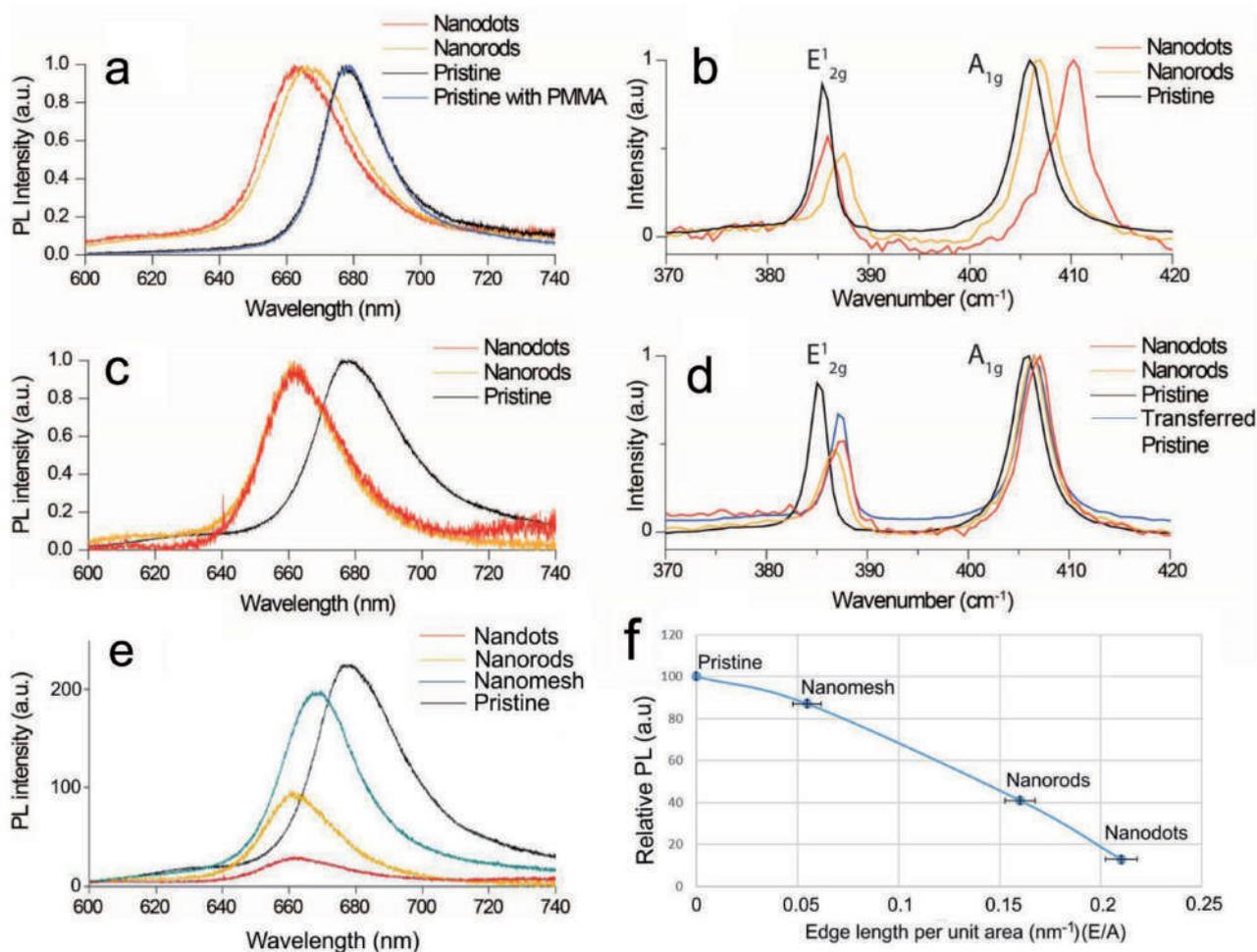
Figure 7. Optical property changes of MoS$_2$ domains induced by nanopatterning. Normalized photoluminescence (PL) a) and Raman b) spectra of monolayer MoS$_2$ nanodots and nanorods before the lift-off process (under an ox-PDMS mask after O$_2$ plasma etching) and those of pristine MoS$_2$ shown for comparison. Normalized PL c) and Raman d) spectra of monolayer MoS$_2$ nanodots and nanorods after the lift-off process and those of as-grown MoS$_2$ domains included for comparison. The Raman spectra of pristine domains transferred onto another SiO$_2$ substrate exhibits similar shifts of both E^1_{2g} and A_{1g} modes to those of nanopatterns. e) Relative PL of nanopatterned and pristine domains after the lift-off process (identical data as shown in (c), normalized to the Raman A_{1g} intensity). f) Plot of the relative PL as a function of the E/A ratio for the 4 different types of MoS$_2$. PL spectra are all normalized to the Raman A_{1g} peak.

and nanorods is decreased to 13% and 42% of the pristine monolayer respectively, which is attributed to the increased defect trapping rate in the nanostructured domains carrying higher edge-to-area ratio. Prior work has shown that the PL quantum efficiency of monolayer MoS$_2$ grown by CVD is typically ≈0.1%.[66] This is also expected for our MoS$_2$ grown by CVD on similar substrates. We therefore use this as the reference value to compare the PL quantum efficiencies of our nanodots (0.013%), nanorods (0.042%) and nanomesh (0.087%). For the nanodots, the edge-to-area ratio (E/A = 4/diameter), is ≈0.21 nm^{-1} for the 18.7 nm dots. For the nanorods we measured typical E/A of 0.16 nm^{-1}, and for the nanomesh E/A of 0.055 nm^{-1}, which indicates that the nanodots have the highest edge density, followed by the nanorods and then nanomesh. Figure 7f plots the relative PL signal as a function of the E/A value for each MoS$_2$ region and shows a nonlinear trend of decreasing PL with increased edge density. This suggests that

the reduction in PL efficiency is associated with increased edge effects, since the ADF-STEM shows all material has the same high quality crystal lattice. The edge region is presumed to have a higher degree of bond disorder than the crystalline interior due to missing nearest neighbor atoms and leads to lower exciton emission intensity as a result of increased quenching.[67] The PL spectra are all normalized to the Raman A_{1g} peak, which takes into account the different PL changes that would arise from the strain shift of absorption spectra. Time-resolved PL experiments were performed on pristine and nanorod MoS$_2$ domains, while the MoS$_2$ nanodots were difficult to measure accurately due to their lower relative PL intensity. The room temperature PL decay from the nanorods was nearly identical to the pristine domain, Figure S6 (Supporting Information), with some convolution from the instrument response function, consistent with previous reports suggesting lifetimes < 1 ns.[68,69]

3. Conclusion

The use of BCP lithography has enabled the fabrication of nanodots, nanorod, and nanomesh features in monolayer MoS_2. The BCP lithography was successful across large scale areas up to 1 cm × 1 cm, and uniform areas of nanodots as large as 2 µm were achieved. The ability to produce micron-scale uniform areas of nanodots, nanorods, and nanomesh enabled their separate probing by photoluminescence and Raman spectroscopy, revealing reduced PL efficiency in nanodots compared to nanorods and nanomesh, which we attribute to increased edge density. Even though nanorods with widths down to 4 nm were present in the samples, no evidence for quantum confinement effect was found, nor in the nanodots that are ≈19 nm. This is expected since the Bohr radius of a monolayer MoS_2 exciton is calculated to be 0.5–1 nm,[70–72] which requires the lateral size reduction of nanodots down to the 1–2 nm scale in order to observe any quantum confinement effect across the 2D plane.[16] These results show that increased edge density causes decreased PL efficiency and that the BCP lithography process results in the release of strain that forms during the CVD growth and cooling process. However, the confirmation that small 19 nm nanodots of MoS_2 still exhibit strong PL is promising for their future implementation in photonic based nanoscale applications. Further work to improve the PL efficiency may involve the functionalization of the edges to reduce quenching in order to enhance their potential impact in future photonic and optoelectronic applications.

4. Experimental Section

Chemical Vapor Deposition Growth of Monolayer MoS_2: MoS_2 monolayers were prepared using a similar approach to that previously reported.[62] Molybdenum trioxide (MoO_3, ≥99.5%, Sigma-Aldrich) and sulfur (S, ≥99.5%, Sigma-Aldrich) powder were used to grow monolayer MoS_2 on a SiO_2/Si substrate (300 nm thick SiO_2) by CVD at atmospheric pressure. Two furnaces were used to enable temperature control on both the precursors. The heating temperatures for S, MoO_3, and SiO_2/Si substrate were ≈180, ≈300, and ≈800 °C, respectively. Argon was used as the carrier gas with a flow rate of 150 sccm. The MoO_3 and S powders were loaded separately in two nested tubes so that the reaction between the precursor vapors was restricted in the vicinity of the substrate placed downstream.

Block Copolymer Patterning and Oxygen Plasma Etching Process: On the substrate with CVD-grown monolayer MoS_2, a 30 nm thick PMMA (950 PMMA, MicroChem, MW = 950 kg mol^{-1}, 0.7% in anisole) was first spin-coated and then baked at 90 °C for 30 s, followed by spin-coating a 35 nm thick PS-*b*-PDMS film (MW = 56 kg mol^{-1}, f_{PDMS} = 16%, 1% in cyclohexane). Then the sample was put in a toluene vapor environment for the annealing process, which allowed the PS-*b*-PDMS to self-assemble into arrays of PDMS spherical microdomains. After annealing, 5 s of CF_4 (50 W) and 60 s of O_2 (90 W) reactive ion etch was applied onto the sample to oxidize PDMS dots (producing a silica-like material which resists O_2 plasma) and to remove the PS/PMMA/MoS_2 layers in the area that was not covered by the oxidized-PDMS.

Scanning Transmission Electron Microscopy: ADF-STEM imaging was conducted using an aberration corrected JEOL ARM300CF STEM equipped with a JEOL ETA corrector operated at an accelerating voltage of 60 kV located in the electron Physical Sciences Imaging Centre (ePSIC) at Diamond Light Source. Dwell times of 5–20 µs and a pixel size of 0.006 nm px^{-1} were typically used for imaging. Optical conditions used a CL aperture of 30 µm, a convergence semi-angle of 31.5 mrad, a beam current of 44 pA, and inner–outer acquisition angles of 49.5–198 mrad. Nanopatterned MoS_2 was transferred from a silicon wafer onto a holey SiN grid that already contained large area monolayer WS_2 crystals grown by CVD. Transfer was achieved using a PMMA support and etching the SiO_2 substrate using NaOH and then washing in water. After transfer to the TEM grid, the PMMA was removed by acetone.

Other Measurements: PL and Raman spectra were acquired using a Horiba LabRAM 800 HR spectrometer equipped with an Ar$^+$ (514.5 nm) excitation source and a Peltier-cooled CCD detector. The laser was focused on the sample with a 400 nm confocal hole using the 100× objective under reflected illumination. The laser spot on the sample was ≈1 µm in diameter and had a power of ≈4 mW at the sample surface. Scanning electron microscopy was performed using a Helios Nanolab 600 and a Zeiss Merlin, operated at 5 kV. Atomic force microscopy was performed using an Agilent 5500 scanning probe microscope in tapping-mode operation.

Supporting Information

Supporting Information is available from the Wiley Online Library or from the author.

Conflict of Interest

The authors declare no conflict of interest.

[1] K. F. Mak, C. Lee, J. Hone, J. Shan, T. F. Heinz, *Phys. Rev. Lett.* **2010**, *105*, 136805.

[2] A. Splendiani, L. Sun, Y. Zhang, T. Li, J. Kim, C.-Y. Chim, G. Galli, F. Wang, *Nano Lett.* **2010**, *10*, 1271.

[3] W. Zhao, Z. Ghorannevis, L. Chu, M. Toh, C. Kloc, P.-H. Tan, G. Eda, *ACS Nano* **2013**, *7*, 791.

[4] H. D. Ha, D. J. Han, J. S. Choi, M. Park, T. S. Seo, *Small* **2014**, *10*, 3858.

[5] X. Zhang, Z. Lai, Z. Liu, C. Tan, Y. Huang, B. Li, M. Zhao, L. Xie, W. Huang, H. Zhang, *Angew. Chem., Int. Ed.* **2015**, *54*, 5425.

[6] H. Huang, C. Du, H. Shi, X. Feng, J. Li, Y. Tan, W. Song, *Part. Part. Syst. Char.* **2015**, *32*, 72.

[7] J. Cai, C. A. Pignedoli, L. Talirz, P. Ruffieux, H. Söde, L. Liang, V. Meunier, R. Berger, R. Li, X. Feng, K. Müllen, R. Fasel, *Nat. Nanotechnol.* **2014**, *9*, 896.

[8] P. Han, K. Akagi, F. Federici Canova, H. Mutoh, S. Shiraki, K. Iwaya, P. S. Weiss, N. Asao, T. Hitosugi, *ACS Nano* **2014**, *8*, 9181.

[9] D. V. Kosynkin, A. L. Higginbotham, A. Sinitskii, J. R. Lomeda, A. Dimiev, B. K. Price, J. M. Tour, *Nature* **2009**, *458*, 872.

[10] L. Jiao, L. Zhang, X. Wang, G. Diankov, H. Dai, *Nature* **2009**, *458*, 877.

[11] A. Morelos-Gómez, S. M. Vega-Díaz, V. J. González, F. Tristán-López, R. Cruz-Silva, K. Fujisawa, H. Muramatsu, T. Hayashi, X. Mi, H. Shi, H. Sakamoto, F. Khoerunnisa, K. Kaneko, B. G. Sumpter, Y. A. Kim, V. Meunier, M. Endo, E. Muñoz-Sandoval, M. Terrones, *ACS Nano* **2012**, *6*, 2261.

[12] R. Cruz-Silva, A. Morelos-Gómez, S. Vega-Díaz, F. Tristán-López, A. L. Elias, N. Perea-López, H. Muramatsu, T. Hayashi, K. Fujisawa, Y. A. Kim, M. Endo, M. Terrones, *ACS Nano* **2013**, *7*, 2192.

[13] H. Jin, M. Ahn, S. Jeong, J. H. Han, D. Yoo, D. H. Son, J. Cheon, *J. Am. Chem. Soc.* **2016**, *138*, 13253.

[14] S. Mukherjee, R. Maiti, A. Midya, S. Das, S. K. Ray, *ACS Photonics* **2015**, *2*, 760.

[15] W. Qiao, S. M. Yan, X. Y. Song, X. Zhang, X. M. He, W. Zhong, Y. W. Du, *Appl. Surf. Sci.* **2015**, *359*, 130.

[16] Z. X. Gan, L. Z. Liu, H. Y. Wu, Y. L. Hao, Y. Shan, X. L. Wu, P. K. Chu, *Appl. Phys. Lett.* **2015**, *106*, 233113.

[17] S. Xu, D. Li, P. Wu, *Adv. Funct. Mater.* **2015**, *25*, 1127.

[18] J. Lin, O. Cretu, W. Zhou, K. Suenaga, D. Prasai, K. I. Bolotin, N. T. Cuong, M. Otani, S. Okada, A. R. Lupini, J.-C. Idrobo, D. Caudel, A. Burger, N. J. Ghimire, J. Yan, D. G. Mandrus, S. J. Pennycook, S. T. Pantelides, *Nat. Nanotechnol.* **2014**, *9*, 436.

[19] X. Liu, T. Xu, X. Wu, Z. Zhang, J. Yu, H. Qiu, J.-H. Hong, C.-H. Jin, J.-X. Li, X.-R. Wang, L.-T. Sun, W. Guo, *Nat. Commun.* **2013**, *4*, 1776.

[20] W. Liu, B. L. Jackson, J. Zhu, C.-Q. Miao, C.-H. Chung, Y. J. Park, K. Sun, J. Woo, Y.-H. Xie, *ACS Nano* **2010**, *4*, 3927.

[21] K. Celebi, J. Buchheim, R. M. Wyss, A. Droudian, P. Gasser, I. Shorubalko, J.-I. Kye, C. Lee, H. G. Park, *Science* **2014**, *344*, 289.

[22] Z. Liao, T. Zhang, M. Gall, A. Dianat, R. Rosenkranz, R. Jordan, G. Cuniberti, E. Zschech, *Appl. Phys. Lett.* **2015**, *107*, 013108.

[23] D. S. Fox, Y. Zhou, P. Maguire, A. O'Neill, C. Ó'Coileáin, R. Gatensby, A. M. Glushenkov, T. Tao, G. S. Duesberg, I. V. Shvets, M. Abid, M. Abid, H.-C. Wu, Y. Chen, J. N. Coleman, J. F. Donegan, H. Zhang, *Nano Lett.* **2015**, *15*, 5307.

[24] M. C. Lemme, D. C. Bell, J. R. Williams, L. A. Stern, B. W. H. Baugher, P. Jarillo-Herrero, C. M. Marcus, *ACS Nano* **2009**, *3*, 2674.

[25] D. C. Bell, M. C. Lemme, L. A. Stern, J. R. Williams, C. M. Marcus, *Nanotechnology* **2009**, *20*, 455301.

[26] H. Liu, S. Hoeppener, U. S. Schubert, *Chem. Phys. Chem.* **2016**, *17*, 2863.

[27] I.-S. Byun, D. Yoon, J. S. Choi, I. Hwang, D. H. Lee, M. J. Lee, T. Kawai, Y.-W. Son, Q. Jia, H. Cheong, B. H. Park, *ACS Nano* **2011**, *5*, 6417.

[28] L. Tapaszto, G. Dobrik, P. Lambin, L. P. Biro, *Nat. Nanotechnol.* **2008**, *3*, 397.

[29] J. G. Son, M. Son, K.-J. Moon, B. H. Lee, J.-M. Myoung, M. S. Strano, M.-H. Ham, C. A. Ross, *Adv. Mater.* **2013**, *25*, 4723.

[30] L. Leibler, *Macromolecules* **1980**, *13*, 1602.

[31] F. S. Bates, G. H. Fredrickson, *Annu. Rev. Phys. Chem.* **1990**, *41*, 525.

[32] C. M. Bates, M. J. Maher, D. W. Janes, C. J. Ellison, C. G. Willson, *Macromolecules* **2014**, *47*, 2.

[33] X. Gu, Z. Liu, I. Gunkel, S. T. Chourou, S. W. Hong, D. L. Olynick, T. P. Russell, *Adv. Mater.* **2012**, *24*, 5688.

[34] M. Park, C. Harrison, P. M. Chaikin, R. A. Register, D. H. Adamson, *Science* **1997**, *276*, 1401.

[35] J. Kamcev, D. S. Germack, D. Nykypanchuk, R. B. Grubbs, C.-Y. Nam, C. T. Black, *ACS Nano* **2013**, *7*, 339.

[36] S. Xiong, L. Wan, Y. Ishida, Y.-A. Chapuis, G. S. W. Craig, R. Ruiz, P. F. Nealey, *ACS Nano* **2016**, *10*, 7855.

[37] H.-C. Kim, S.-M. Park, W. D. Hinsberg, *Chem. Rev.* **2010**, *110*, 146.

[38] X. Liang, S. Wi, *ACS Nano* **2012**, *6*, 9700.

[39] S.-J. Jeong, S. Jo, J. Lee, K. Yang, H. Lee, C.-S. Lee, H. Park, S. Park, *Nano Lett.* **2016**, *16*, 5378.

[40] J. Lee, K. Kim, W. I. Park, B.-H. Kim, J. H. Park, T.-H. Kim, S. Bong, C.-H. Kim, G. Chae, M. Jun, Y. Hwang, Y. S. Jung, S. Jeon, *Nano Lett.* **2012**, *12*, 6078.

[41] J. W. Bai, X. Zhong, S. Jiang, Y. Huang, X. F. Duan, *Nat. Nanotechnol.* **2010**, *5*, 190.

[42] T. P. Loginova, Y. A. Kabachii, S. N. Sidorov, D. N. Zhirov, P. M. Valetsky, M. G. Ezernitskaya, L. V. Dybrovina, T. P. Bragina, O. L. Lependina, B. Stein, L. M. Bronstein, *Chem. Mater.* **2004**, *16*, 2369.

[43] W. Wei, L. Samad, J. W. Choi, Y. Joo, A. Way, M. S. Arnold, S. Jin, P. Gopalan, *Chem. Mater.* **2016**, *28*, 4017.

[44] K. W. Gotrik, A. F. Hannon, J. G. Son, B. Keller, A. Alexander-Katz, C. A. Ross, *ACS Nano* **2012**, *6*, 8052.

[45] K.-H. Tu, W. Bai, G. Liontos, K. Ntetsikas, A. Avgeropoulos, C. A. Ross, *Nanotechnology* **2015**, *26*, 375301.

[46] S. Yim, D. M. Sim, W. I. Park, M.-J. Choi, J. Choi, J. Jeon, K. H. Kim, Y. S. Jung, *Adv. Funct. Mater.* **2016**, *26*, 5631.

[47] J. G. Son, A. F. Hannon, K. W. Gotrik, A. Alexander-Katz, C. A. Ross, *Adv. Mater.* **2011**, *23*, 634.

[48] C.-C. Chao, T.-C. Wang, R.-M. Ho, P. Georgopanos, A. Avgeropoulos, E. L. Thomas, *ACS Nano* **2010**, *4*, 2088.

[49] N. L. Y. Wu, K. D. Harris, J. M. Buriak, *ACS Nano* **2013**, *7*, 5595.

[50] B. M. D. O'Driscoll, R. A. Kelly, M. Shaw, P. Mokarian-Tabari, G. Liontos, K. Ntetsikas, A. Avgeropoulos, N. Petkov, M. A. Morris, *Eur. Polym. J.* **2013**, *49*, 3445.

[51] Y. S. Jung, J. B. Chang, E. Verploegen, K. K. Berggren, C. A. Ross, *Nano Lett.* **2010**, *10*, 1000.

[52] I. F. Hsieh, H.-J. Sun, Q. Fu, B. Lotz, K. A. Cavicchi, S. Z. D. Cheng, *Soft Matter* **2012**, *8*, 7937.

[53] K. He, A. W. Robertson, Y. Fan, C. S. Allen, Y-C. Lin, K. Suenaga, A. I. Kirkland, J. H. Warner, *ACS Nano* **2015**, *9*, 4786.

[54] W. Zhou, X. Zou, S. Najmaei, Z. Liu, Y. Shi, J. Kong, J. Luo, P. M. Ajayan, B. I. Yakobson, J.-C. Idrobo, *Nano Lett.* **2013**, *13*, 2615.

[55] M. Bollinger, K. Jacobsen, J. Nørskov, *Phys. Rev. B* **2003**, *67*, 085410.

[56] S. Helveg, J. V. Lauritsen, E. Laegsgaard, I. Stensgaard, J. K. Norskov, B. S. Clausen, H. Topsoe, F. Besenbacher, *Phys. Rev. Lett.* **2000**, *84*, 951.

[57] L. P. Hansen, Q. M. Ramasse, C. Kisielowski, M. Brorson, E. Johnson, H. Topsoe, S. Helveg, *Angew. Chem., Int. Ed.* **2011**, *50*, 10153.

[58] H. R. Gutiérrez, N. Perea-Lopez, A. L. Elias, A. Berkdemir, B. Wang, R. Lv, F. Lopez-Urias, V. H. Crespi, H. Terrones, M. Terrones, *Nano Lett.* **2013**, *13*, 3447.

[59] H. J. Conley, B. Wang, J. I. Ziegler, R. F. Haglund, S. T. Pantelides, K. I. Bolotin, *Nano Lett.* **2013**, *13*, 3626.

[60] Y. Wang, C. Cong, C. Qiu, T. Yu, *Small* **2013**, *9*, 2857.

[61] S. Huang, X. Ling, L. Liang, J. Kong, H. Terrones, V. Meunier, M. S. Dresselhaus, *Nano Lett.* **2014**, *14*, 5500.

[62] S. Wang, X. Wang, J. H. Warner, *ACS Nano* **2015**, *9*, 5246.

[63] B. Chakraborty, A. Bera, D. V. S. Muthu, S. Bhowmick, U. V. Waghmare, A. K. Sood, *Phys. Rev. B* **2012**, *85*, 161403.

[64] N. Mao, Y. Chen, D. Liu, J. Zhang, L. Xie, *Small* **2013**, *9*, 1312.

[65] W. M. Parkin, A. Balan, L. Liang, P. M. Das, M. Lamparski, C. H. Naylor, J. A. Rodríguez-Manzo, A. T. C. Johnson, V. Meunier, M. Drndić, *ACS Nano* **2016**, *10*, 4134.

[66] M. Amani, R. A. Burke, X. Ji, P. Zhao, D-H. Lien, P. Taheri, G. H. Ahn, D. Kirya, J. W. Agar III, E. Yablonovitch, J. Kong, M. Dubey, A. Javey, *ACS Nano* **2016**, *10*, 6535.

[67] W. Bao, N. J. Borys, C. Ko, J. Suh, W. Fan, A. Thron, Y. Zhang, A. Buyanin, J. Zhang, S. Cabrini, P. D. Ashby, A. Weber-Bargioni, S. Tongay, S. Aloni, D. F. Ogletree, J. Wu, M. B. Salmeron, P. J. Schuck, *Nat. Commun.* **2015**, *6*, 7993.

[68] M. Palummo, M. Bernardi, J. C. Grossman, *Nano Lett.* **2015**, *15*, 2794.

[69] H. Shi, R. Yan, S. Bertolazzi, J. Brivio, B. Gao, A. Kis, D. Jena, H. G. Xing, L. Huang, *ACS Nano* **2013**, *7*, 1072.

[70] G. Y. Jia, Y. Liu, J. Y. Gong, D. Y. Lei, D. L. Wang, Z. X. Huang, *J. Mater. Chem. C* **2016**, *4*, 8822.

[71] Y. Yu, Y. Yu, Y. Cai, W. Li, A. Gurarslan, H. Peelaers, D. E. Aspnes, C. G. Van de Walle, N. V. Nguyen, Y.-W. Zhang, L. Cao, *Sci. Rep.* **2015**, *5*, 16996.

[72] T. Cheiwchanchamnangij, W. R. L. Lambrecht, *Phys. Rev. B* **2012**, *85*, 205302.